MDPI

Article

A Novel Two-Dimensional ZnSiP$_2$ Monolayer as an Anode Material for K-Ion Batteries and NO$_2$ Gas Sensing

Chunying Pu [1], Zhuo Wang [2], Xin Tang [3] , Dawei Zhou [1],*, and Jinbing Cheng [1],*

[1] Henan International Joint Laboratory of MXene Materials Microstructure, College of Physics and Electronic Engineering, Nanyang Normal University, Nanyang 473061, China
[2] College of mechanical and electrical engineering, Nanyang Normal University, Nanyang 473061, China
[3] College of Material Science and Engineering, Guilin University of Technology, Guilin 541004, China
* Correspondence: zhoudawei@nynu.edu.cn (D.Z.); chengjinbing1988@163.com (J.C.)

Abstract: Using the crystal-structure search technique and first-principles calculation, we report a new two-dimensional semiconductor, ZnSiP$_2$, which was found to be stable by phonon, molecular-dynamic, and elastic-moduli simulations. ZnSiP$_2$ has an indirect band gap of 1.79 eV and exhibits an anisotropic character mechanically. Here, we investigated the ZnSiP$_2$ monolayer as an anode material for K-ion batteries and gas sensing for the adsorption of CO, CO$_2$, SO$_2$, NO, NO$_2$, and NH$_3$ gas molecules. Our calculations show that the ZnSiP$_2$ monolayer possesses a theoretical capacity of 517 mAh/g for K ions and an ultralow diffusion barrier of 0.12 eV. Importantly, the ZnSiP$_2$ monolayer exhibits metallic behavior after the adsorption of the K-atom layer, which provides better conductivity in a period of the battery cycle. In addition, the results show that the ZnSiP$_2$ monolayer is highly sensitive and selective to NO$_2$ gas molecules.

Keywords: two-dimensional ZnSiP$_2$; first-principles calculations; K-ion batteries; gas sensing

1. Introduction

Two-dimensional semiconductor (2D) materials have potential applications in electronic equipment, catalysis, electrode materials, and gas sensors owing to their significant electrical, physical, and chemical properties [1–4]. In particular, the large surface areas, excellent mechanical strengths, and strong surface activities of 2D materials provide excellent advantages for the adsorption of certain metal atoms and gas molecules, which make 2D materials suitable as anodes for metal-ion batteries and gas sensors [5,6]. Recently, many novel 2D semiconductors [7–18] have attracted much attention due to their high stabilities, good electronic properties, high capacities for metal-ion batteries, and high sensitivities toward certain gases, such as NO$_2$, SO$_2$, and NH$_3$.

As a new family of 2D materials, phosphorus carbides (PCs) with α phase and β phase are semiconductors that exhibit highly anisotropic electronic characters with high carrier mobilities. More importantly, α-PC and β-PC, as promising anode materials for Li-, Na-, and K-ion batteries, having high capacities and fast diffusion channels for Li, Na, and K ions [10,11]. It has also been predicted that α-PC, as a promising gas sensor, exhibits superior selectivity and sensitivity for NO$_2$ [12]. Buckled-graphene-like PC$_6$, as a semiconductor, has been predicted to have ultrahigh carrier mobility and, as an anode for Li-ion batteries, a high capacity of 717 mAh/g and an open-circuit voltage of 0.21 V [13]. Furthermore, typical 2D metal-phosphide δ-InP$_3$ exhibits high electron mobility and has been shown to be usable as a N-based gas sensor with high selectivity and sensitivity and good reversibility [16]. In addition, metal oxides, such as two-dimensional WO$_3$ and Pd-loaded ZnO monolayers, are important semiconductors applied in gas sensors, with high sensitivities [19,20].

Apart from the excellent performances of binary semiconductors, ternary 2D semiconductor materials have also attracted special interest. Using the epitaxial growth technique,

Beniwal and co-workers [21] synthesized a 2D hexagonal graphenic BCN monolayer, which showed semiconductor behavior with a band gap of 1.50 eV, high directional anisotropy, a small Young's modulus, high flexibility, and suitability as a potential electrode material for Al-based dual-ion batteries [22]. Recently, a new semiconductor BCN structure, by the global-optimization search method, was predicted to have high carrier mobility and excellent optical properties [23]. Using first-principles simulations, two-dimensional BC_2P and BC_3P_3 monolayers were also predicted to present semiconductors with proper band gaps and low barriers for the dissociation of water and hydrogen molecules and thus to show promise for use in renewable energy [24]. Recently, Tang et al. [25] designed a BC_6P monolayer isostructural and isoelectronic to graphene that has high electron mobility and can be used in K-ion batteries, with a high capacity of 1410 mAh/g.

In recent years, we have noticed that the bulk ternary chalcopyrite-structure compound $ZnSiP_2$ is a promising semiconductor that has been synthesized experimentally [26,27] and used for optical, optoelectronic, photovoltaic, and thermoelectric applications [28–31]. However, its 2D structure is still unclear and has not been studied. In this paper, we predicted a stable structure of the 2D semiconductor $ZnSiP_2$ and studied its electronic, mechanical properties as well as its electrode performance for K-ion batteries (KIBs). $ZnSiP_2$, as an electrode for K-ion batteries, has a high theoretical storage capacity of 517 mAh/g and a low diffusion energy of 0.12 eV. In addition, its gas-sensing performance was investigated by simulation of the adsorption of CO, CO_2, SO_2, NO, NO_2, and NH_3 gas molecules on the $ZnSiP_2$ monolayer. Our calculation results demonstrate that the strong adsorption ability with respect to K ions and NO_2 gas molecules on the $ZnSiP_2$ monolayer makes it a promising anode for K-ion batteries and gas sensors for NO_2.

2. Results and Discussion

2.1. Structure and Stability

By using the global-structure search method, we found a new $ZnSiP_2$ monolayer with the space group Pmc21 (no. 26) containing two formula units. The structure crystalized in an orthorhombic structure, and the optimized lattice parameters were a = 3.7251 and b = 6.1398 Å. As shown in Figure 1a, a remarkable feature is that the $ZnSiP_2$ monolayer is stacked as a bilayer hexagonal lattice, and the two layers are bonded by Si and P, with a distance of 2.286 Å. Each layer was arranged alternately in two kinds of hexagonal rings. One ring was composed of one Si, two Zn, and three P atoms; the other ring was composed of one Zn, two Si, and three P atoms, which gave rise to two types of bonds: Si-P and Zn-P. To understand the chemical-bonding nature, the charge density difference was calculated and shown in Figure 1b, which is defined as the difference between the total electron density of the $ZnSiP_2$ monolayer and the charge density of isolated Zn, Si, and P atoms at their specified positions. It can clearly be seen that there is a strong non-polar covalent bond between Si and P [32]. Regarding the Zn-P bonds, the polar covalent bonds between Zn and P atoms were due to the transfer charges shifted toward P atoms.

The cohesive energy is a key factor in experimental synthesis, which is calculated by $E_{coh} = (2E_{Si} + 2E_{Zn} + 4E_P - E_{ZnSiP_2})/8$, where E_{Si}, E_{Zn}, E_P, and E_{ZnSiP_2} represent the energies of one Si, Zn, P, and perfect $ZnSiP_2$, respectively. The calculated cohesive energy of the $ZnSiP_2$ monolayer was 4.36 eV/atom, which is comparable to those of phophorene (3.30 eV/atom) [33], germanene (3.26 eV/atom), silicene (3.98 eV/atom) [34], and SiP (4.16 eV/atom) [35]. We further calculated the formation energy of the $ZnSiP_2$ monolayer related to the SiP_2 monolayer and Zn metal to investigate its stability, which was calculated by $E_f = E_{ZnSiP_2} - \mu_{SiP_2} - m\mu_{Zn(bulk)}$, where μ_{SiP_2}, $\mu_{Zn(bulk)}$, and E_{ZnSiP_2} are the energies of two-dimensional SiP_2 [36], one Zn atom in bulk Zn metal, and the perfect $ZnSiP_2$ monolayer, respectively, and m is the number of Zn atoms. The calculated formation energy is −0.465 eV, the negative value further indicating that the $ZnSiP_2$ monolayer may be synthesized. The phonon spectrum was used to check the dynamic stability of the $ZnSiP_2$ monolayer. The calculated phonon dispersion curves for the $ZnSiP_2$ monolayer are shown in Figure 2a; all frequencies in the Brillouin region were positive, which means

that the ZnSiP$_2$ monolayer is dynamically stable. Furthermore, thermal stability was checked by AIMD simulation running for 10 ps at 400 K (Figure 2b); the structure remained almost intact at the end of the simulation, revealing that the ZnSiP$_2$ monolayer has good thermal stability. According to the above analysis, the predicted 2D ZnSiP$_2$ is promising for experimental synthesis.
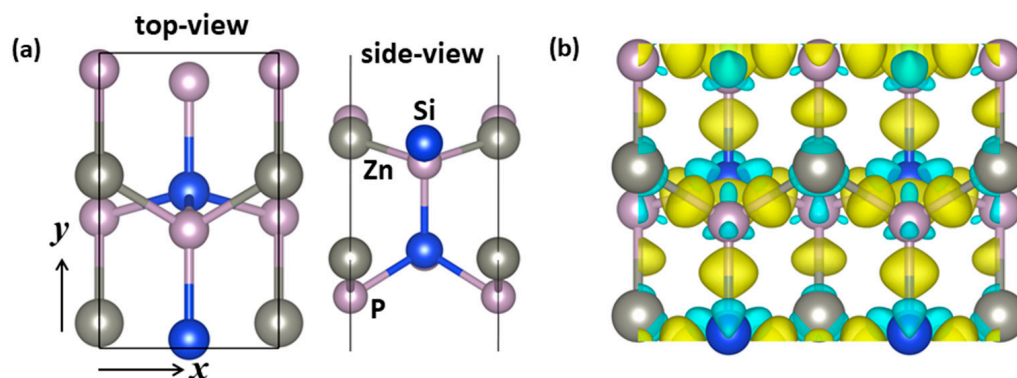

Figure 1. (**a**) The lowest-energy geometry of the ZnSiP$_2$ monolayer, with top and side views.(**b**) The charge density difference of the ZnSiP$_2$ monolayer. (The gold coloring (i.e., 0.01 e/Å^3) in the plot indicates an electron-density increase after bonding, and the cyan coloring (i.e., 0.01 e/Å3) indicates a decrease.) Zn atoms are gray, Si atoms blue and P atoms pink.
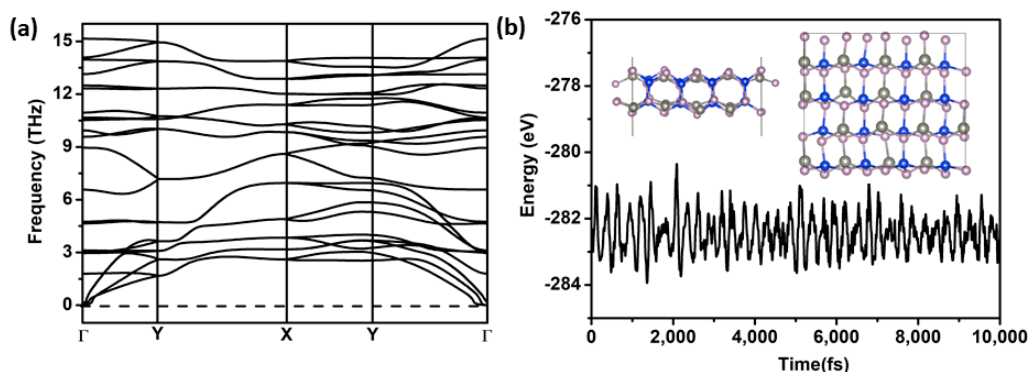
Figure 2. (**a**) The phonon spectra of the ZnSiP$_2$ monolayer. (**b**) Vibration of total potential energy of ZnSiP$_2$ during the AIMD (400 K). The inset is the final snapshot of ZnSiP$_2$ at the end of 10 ps.

Additionally, we further calculated the four independent elastic constants of the ZnSiP$_2$ monolayer, which were C$_{11}$ = 106.2 Nm^{-1}, C$_{22}$ = 86.0 Nm^{-1}, C$_{12}$ = 8.6 Nm^{-1}, and C$_{44}$ = 26.1 Nm^{-1}. According to the obtained elastic constants, the ZnSiP$_2$ monolayer satisfied the mechanical stability standard: C$_{11}$ > 0; C$_{44}$ > 0; C$_{11}$C$_{22}$ > C$_{12}^2$ [37]. Moreover, the diagrams for the in-plane Young's modulus and Poisson ratio with polar angle [38] could be obtained and are depicted in Figure 3, showing that the ZnSiP$_2$ monolayer is anisotropic. The maximum Young's modulus (105 N/m) was higher than that reported for phosphorene (92 N/m) [39] and comparable to those of MoS$_2$ (129 N/m) [40] and V$_2$Te$_2$O monolayers (115.3 N/m) [41]. The anisotropy characteristic of mechanical properties also has an important effect on electronic properties.
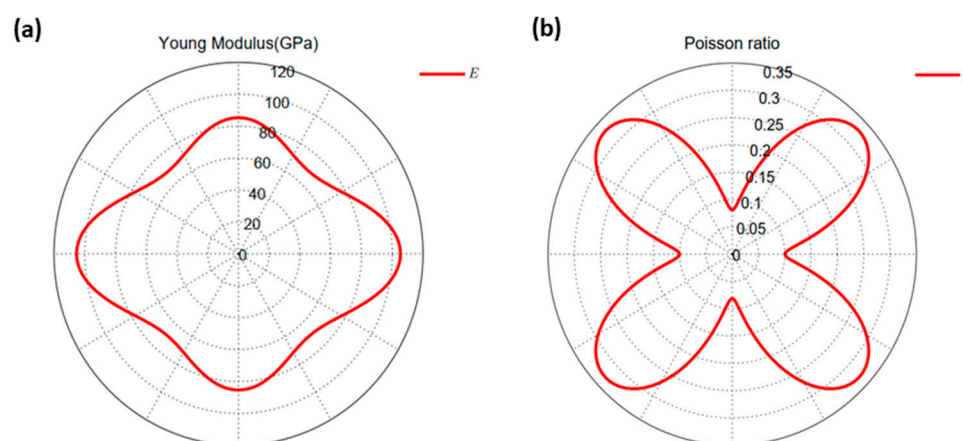
Figure 3. Directional dependences of (**a**) Young's modulus, E, and (**b**) Poisson's ratio, υ.

2.2. Electronic and Adsorption Properties

The calculated band structure and density of states for the $ZnSiP_2$ monolayer are shown in Figure 4a,b. The valence band maximum (VBM) is at point Γ, and the conduction band minimum (CBM) is at point Y. Therefore, as an indirect semiconductor, the band-gap values derived from the PBE and HSE calculations were 1.04 and 1.79 eV, respectively. The band dispersion near the VBM and CBM shows an anisotropic character, which results in the anisotropy of the effective masses. According to the formula $m^* = \frac{\hbar^2}{\partial E^2/\partial k^2}$, the obtained electron effective masses near the CBM were 1.364 m_0 and 0.333 m_0 along the x-and y-directions, while the hole effective masses near the VBM were 1.019 m_0 and 0.433 m_0 along the x- and y-directions, respectively. The density of states in Figure 4b shows that the VBM and CBM are both mainly contributed to by P 2p and Zn 4d orbitals.
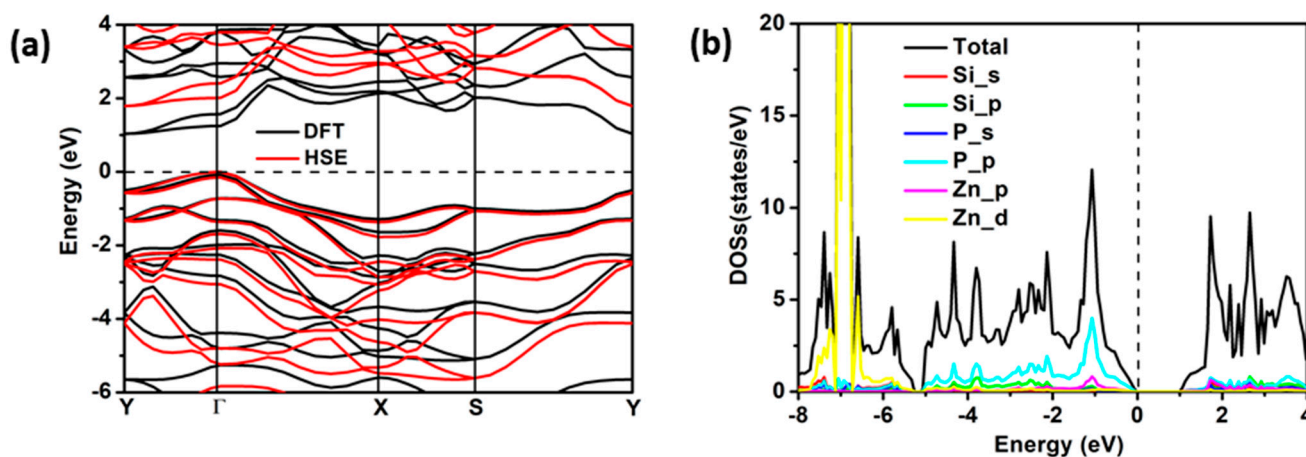
Figure 4. (**a**) The band structure (DFT-PBE and HSE functionals) and (**b**) density of states (PBE functional) for the $ZnSiP_2$ monolayer.

To further study the performance of the $ZnSiP_2$ monolayer as an electrode material, we investigated the adsorption properties of one K atom on its surface using a $3 \times 2 \times 1$ supercell as the substrate. According to the structural symmetry, ten possible K-atom adsorption sites (S1–S10) with adsorption energies based on Equation (1) were considered and calculated, as shown in Figure 5. After geometric-structure optimization, we found some equivalent sites due to the transfer of K atoms from one site to another site. As can be clearly seen in Figure 5b, the equivalent sites were $S_1 = S_2 = S_3 = S_9 = S_{10}$ and $S_5 = S_7 = S_8$, so only four sites S_2, S_4, S_5, and S_6 were left, with adsorption energies of −0.68, −0.57, −0.55, and −0.35 eV, respectively. Thus, the adsorption energy of the K atom at S_2 site was the lowest, which means that the adsorbed K atoms prefer to stay at the bridge position of

Si-P to reduce the Coulomb repulsion between K and Zn. The nearest K-P, K-Zn and K-Si distances are 3.30 Å, 3.92 Å and 3.53 Å, respectively.
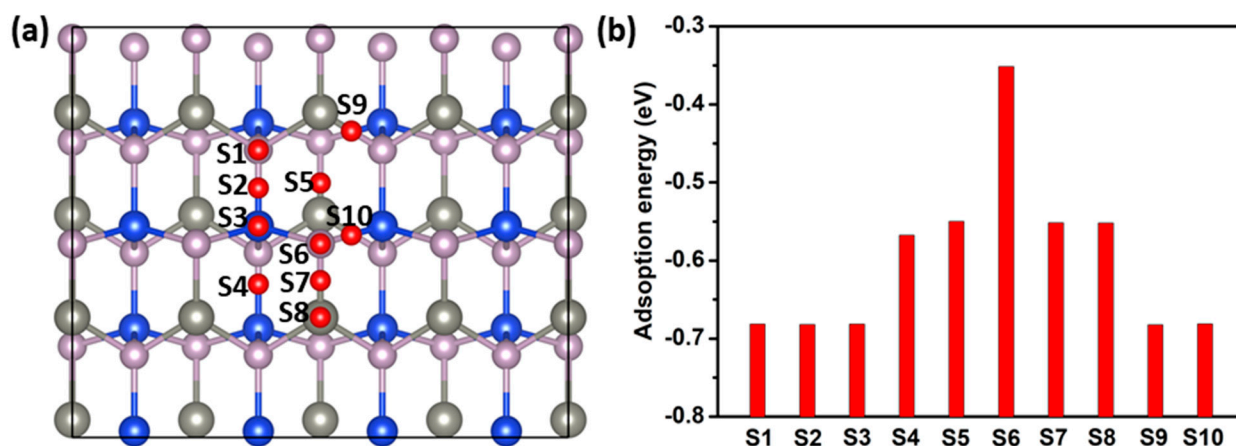

Figure 5. (**a**) S1–S10 are the possible adsorption configurations of K ions on the ZnSiP$_2$ monolayer. (**b**) Adsorption energies of K ions at each location.

To assess the adsorption behavior of the K atoms, we calculated the charge-density differences shown in Figure 6a, which is defined by:

$$\Delta\rho = \rho(\text{KZn}_{12}\text{Si}_{12}\text{P}_{24}) - \rho(\text{K}) - \rho(\text{Zn}_{12}\text{Si}_{12}\text{P}_{24})$$

where $\rho(\text{Zn}_{12}\text{Si}_{12}\text{P}_{24})$, $\rho(\text{KZn}_{12}\text{Si}_{12}\text{P}_{24})$, and $\rho(\text{K})$ are the charge densities of the $\text{Zn}_{12}\text{Si}_{12}\text{P}_{24}$ monolayer with adsorbed K atoms, the substrate $\text{Zn}_{12}\text{Si}_{12}\text{P}_{24}$, and an isolated K atom, respectively. Obvious charge transfer could be observed, and the K atoms had a net charge of $0.84^{|e|}$ based on the Bader charge analysis, which implies charge transfer from the K atoms to the adjacent P and Si atoms in the $\text{Zn}_{12}\text{Si}_{12}\text{P}_{24}$ surface.
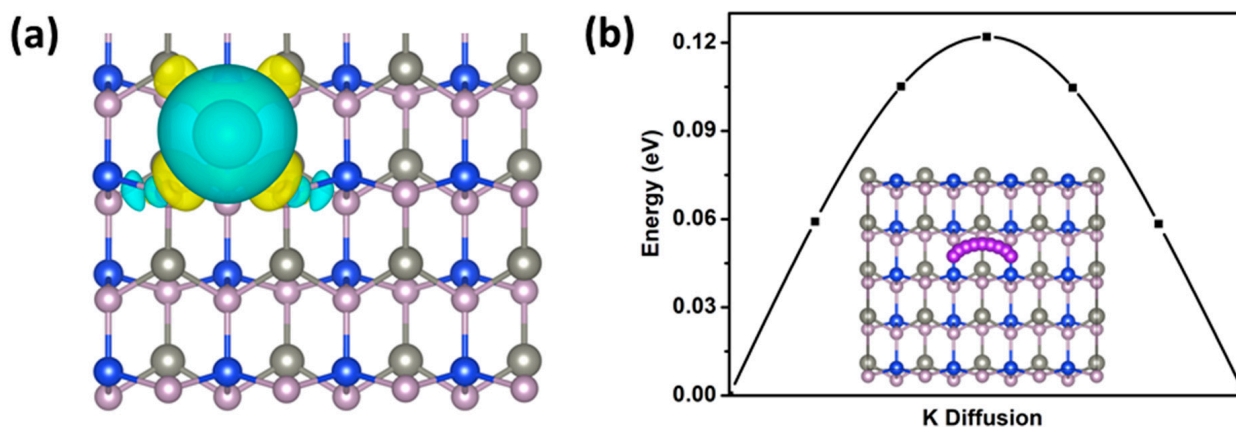
Figure 6. (**a**)The charge density difference with the adsorption of K atom with the isosurface level of 0.01 e/Å^3. (**b**) Energy profile for the diffusion of K on the surface of ZnSiP$_2$ monolayer along the path of the inset. The purple ball represents the K atom.

The diffusion barrier of K ions is a key parameter in estimating the performance of a battery. Next, the diffusion of one K ion on the ZnSiP$_2$ surface was investigated. The possible diffusion path (inset of Figure 6b) between the lowest-energy adsorption sites and the calculated results is shown in Figure 6b. The diffusion barrier of the path was 0.12 eV, which is comparable to the result for ReN$_2$ (0.127 eV) [42]. Compared with other anode materials, ZnSiP$_2$ has a low K-ion diffusion barrier that is smaller than those of BP (0.155 eV) [43], PC$_6$ (0.26 eV) [44], and SnC (0.17 eV) [45]. However, this value is larger

than those of GeS (0.05 eV) [46], Ti_3C_2 (0.103 eV) [47], and C_6BN (0.087 eV) [48]. The low diffusion barrier can result in ultrafast charging–discharging cycles in K-ion batteries.

2.3. Capacity and Open-Circuit Voltage

After studying the adsorption and diffusion behavior of one K atom on the supercell of the $ZnSiP_2$ monolayer, we then explored the behavior of K adsorption concentration. Five K concentrations ($K_xZn_2Si_2P_4$, x = 1–4, 6) were considered, and the average adsorption energies acquired according to Equation (2) were −0.30, −0.46, −0.16, −0.12, and −0.03 eV, respectively. It is to be noted that the K concentration reached x = 6, still showing negative adsorption energy, which means that K atoms can be adsorbed on the $ZnSiP_2$ monolayer. The three stable adsorption configurations ($K_2Zn_2Si_2P_4$, $K_4Zn_2Si_2P_4$, and $K_6Zn_2Si_2P_4$) are shown in the inset of Figure 7. The first and the second K atom layers are located at S_2 and S_5 sites, with both sides of the $ZnSiP_2$ monolayer. As for the third K-atom layer, the K atom prefers to stay at the S_2 site. The stoichiometry $K_6Zn_2Si_2P_4$ can provide the maximal storage capacity 517 mAh/g, according to Equation (4), which is higher than other reported values for 2D materials, such as GeS (256 mAh/g) [46], ReN_2 (250 mAh/g) [42], Ti_3C_2 (191 mAh/g) [47], MoS_2/Ti_2CS_2 (141 mAh/g) [49], and MoN_2 (432 mAh/g) [50], but lower than the capacities for BC_3 (858 mAh/g) [51], BC_6P (1410 mAh/g) [25], C_6BN (533 mAh/g) [48], BP (570 mAh/g) [43], and V_2S_2O (883.6Ah/g) [41]. Based on Equation (3), OCVs were obtained and are shown in Figure 7, and the calculated values for different concentrations, $KZn_2Si_2P_4$, $K_2Zn_2Si_2P_4$, $K_3Zn_2Si_2P_4$, $K_4Zn_2Si_2P_4$, and $K_6Zn_2Si_2P_4$, were 0.30, 0.46, 0.16, 0.12, and 0.03 V, respectively. The Bader analysis showed that every K atom transfers 0.58 e to $ZnSiP_2$ when two K atoms are absorbed on the surface of 2D $ZnSiP_2$, while every K atom transfers 0.51 e to $ZnSiP_2$ when only one K atom is absorbed on the surface of 2D $ZnSiP_2$, implying that two K atoms are more easily absorbed on the surface of 2D $ZnSiP_2$ than one K atom. So, the OCV increases as x increases from 1 to 2, as shown in Figure 7. However, the overall voltage decreases as the capacity increases.
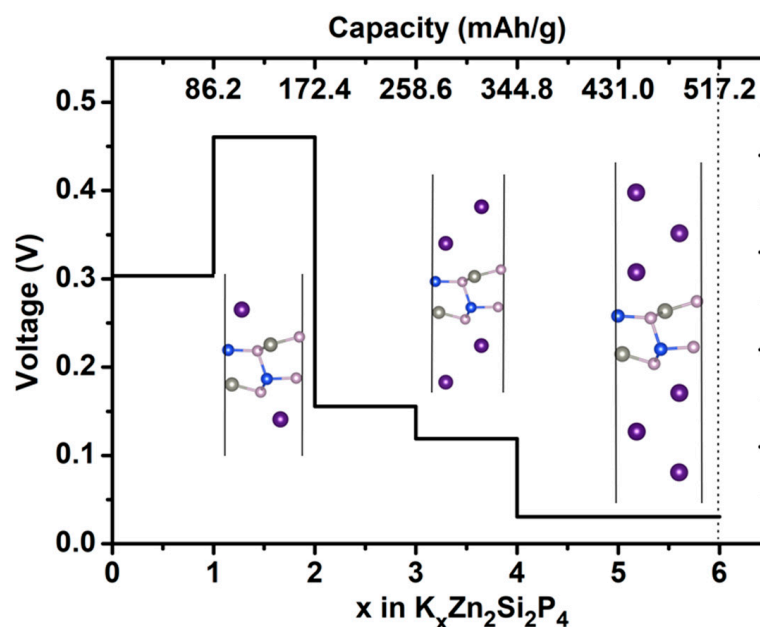
Figure 7. Predicted voltage as a function of capacity and K content (x) in $K_xZn_2Si_2P_4$.

Importantly, the density states of the three stable adsorption configurations ($KZn_2Si_2P_4$, $K_2Zn_2Si_2P_4$, and $K_3Zn_2Si_2P_4$) were calculated using the PBE functional, and $ZnSiP_2$, after the adsorption of K atoms, showed metallic behavior, as shown in Figure 8, which is beneficial for the $ZnSiP_2$ monolayer as an electrode material.
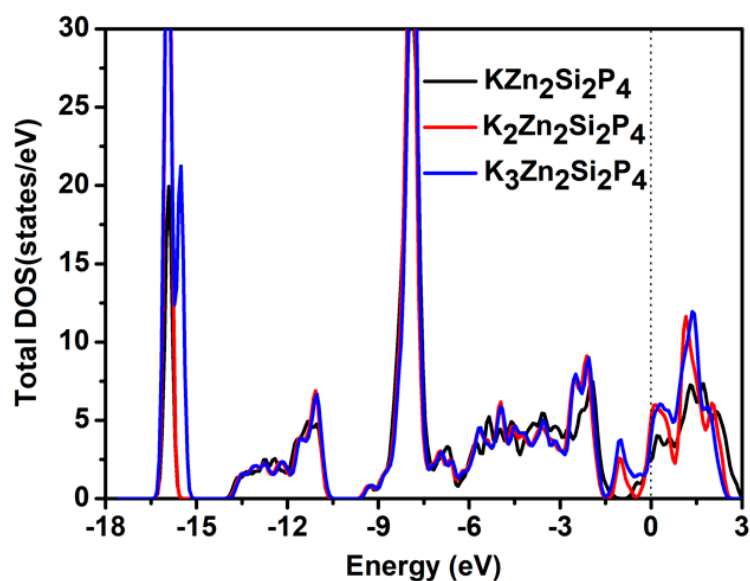
Figure 8. The total densities of states of $KZn_2Si_2P_4$, $K_2Zn_2Si_2P_4$, and $K_3Zn_2Si_2P_4$.

2.4. Gas-Sensing Properties

To further study the gas-sensing ability of the $ZnSiP_2$ monolayer, we systematically studied the adsorption behavior of gas molecules (CO, CO_2, SO_2, NO, NO_2, and NH_3) on its surface by first-principles simulations. The most stable configurations of the gas molecules adsorbed on the $ZnSiP_2$ monolayer are shown in Figure 9, and the corresponding adsorption energies (E_{ad}), adsorption distances (d_0), band gaps after molecule adsorption (E_g), and charge transfers (Q) are listed in Table 1. A positive charge for Q means charge transfer from the monolayer to the gas molecules. The equilibrium distance of 1.53 Å between NO_2 and the monolayer revealed that NO_2 forms a stable chemical bond. Moreover, the NO_2 molecules showed high adsorption energies, indicating that $ZnSiP_2$ is more sensitive to NO_2 molecules than the other five molecules. As shown in Table 1, the Bader charge analysis indicated that there were 0.24, 0.12, 0.67, and 0.13 electron transfers between the molecules and the substrates for SO_2, NO, NO_2, and NH_3, which further implies that NO_2 molecules have strong chemical interactions with the $ZnSiP_2$ monolayer.

Table 1. The adsorption energy, equilibrium distance, energy band gap, and charge transfer for different gas molecules adsorbed on the $ZnSiP_2$ monolayer.

Molecule	CO	CO_2	SO_2	NO	NO_2	NH_3
E_{ad} (eV)	−0.74	−0.55	−1.09	−0.75	−1.30	−1.14
d_0 (Å)	1.54	2.29	1.73	1.68	1.53	1.53
E_g (eV)	1.04	1.04	0.9	metal	metal	1.04
Q (e)	0	0	−0.24	0.12	0.67	−0.13

The electronic band structures and densities of states for gas-$ZnSiP_2$ are shown in Figures 10 and 11, respectively. All the systems, except for NO and NO_2, that adsorbed the $ZnSiP_2$ monolayer became direct band-gap semiconductors, and both VBM and CBM were at the Gamma point. It can be clearly seen from Figures 10 and 11 that the NO and NO_2 adsorbed on the $ZnSiP_2$ monolayer introduced a high density of states at the Fermi surface, which made the $ZnSiP_2$ exhibit a metallic character and changed the electronic properties of the $ZnSiP_2$ monolayer easily. The adsorption of CO, CO_2, and NH_3 had no significant effect on the band structure, and the band gaps did not change much. For SO_2 adsorption (see Figure 10c), the shallow donor energy levels were introduced into the energy band, resulting in the narrowing of the band gap. Combining all the above results, we can conclude that the $ZnSiP_2$ monolayer is promising as a sensor of NO_2 gas molecules with high selectivity and sensitivity.
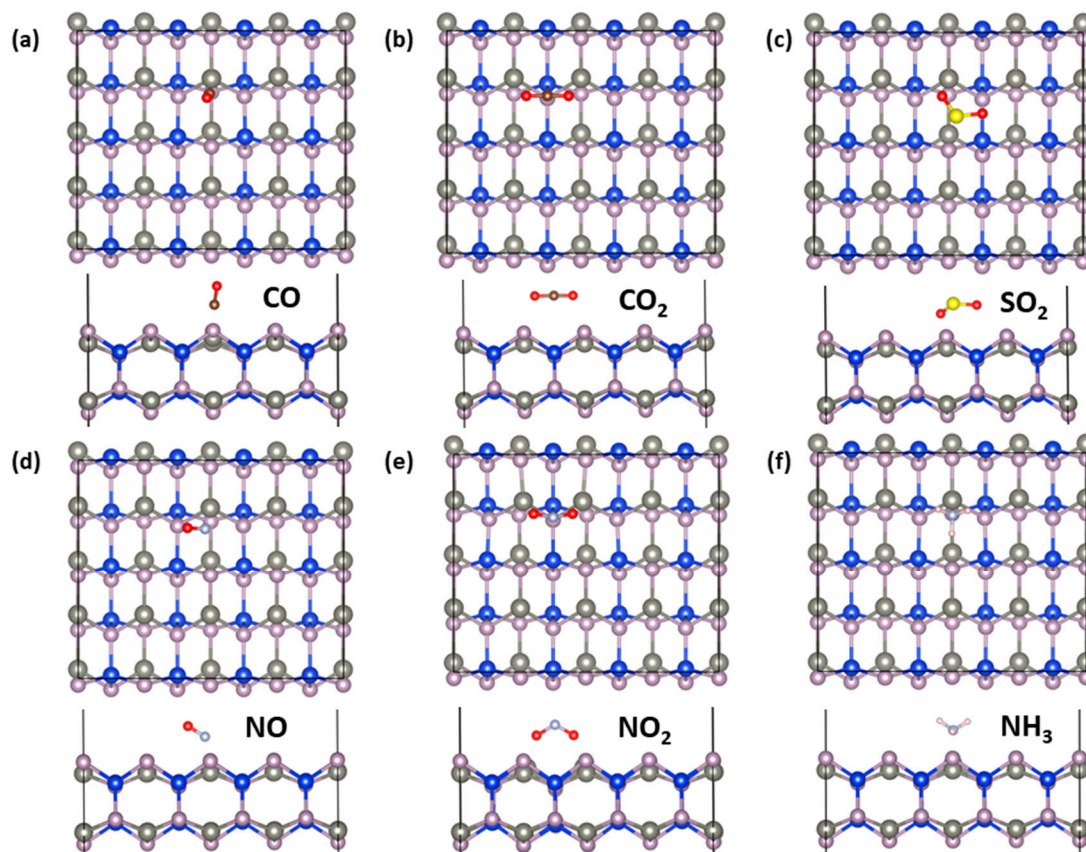
Figure 9. Top and side views of the most stable adsorption of the small gas molecules (**a**) CO, (**b**) CO_2, (**c**) SO_2, (**d**) NO, (**e**) NO_2, and (**f**) NH_3 on the $ZnSiP_2$ monolayer. (The gray, brown, red, yellow, and pink balls represent N, C, O, S, and H atoms, respectively.)
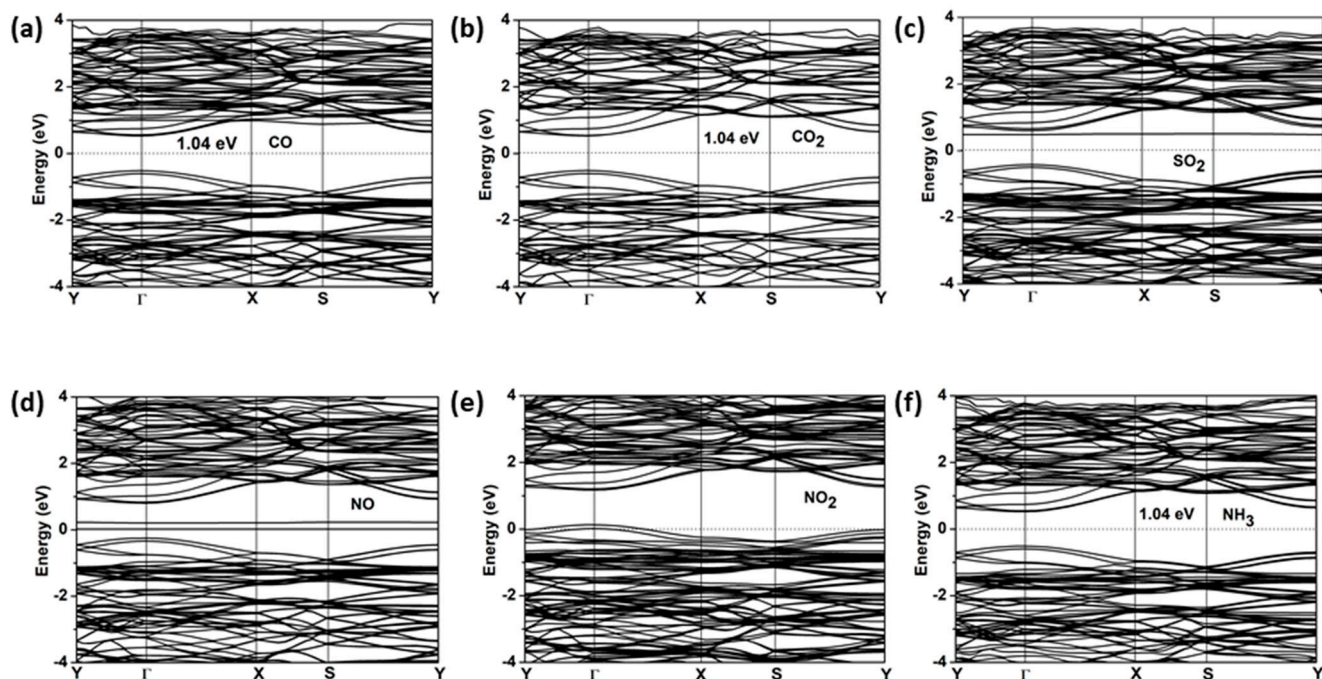
Figure 10. The electronic band structures (PBE functional) for the stable structures of: (**a**) CO, (**b**) CO_2, (**c**) SO_2, (**d**) NO, (**e**) NO_2, and (**f**) NH_3 adsorbed on the $ZnSiP_2$ monolayer.
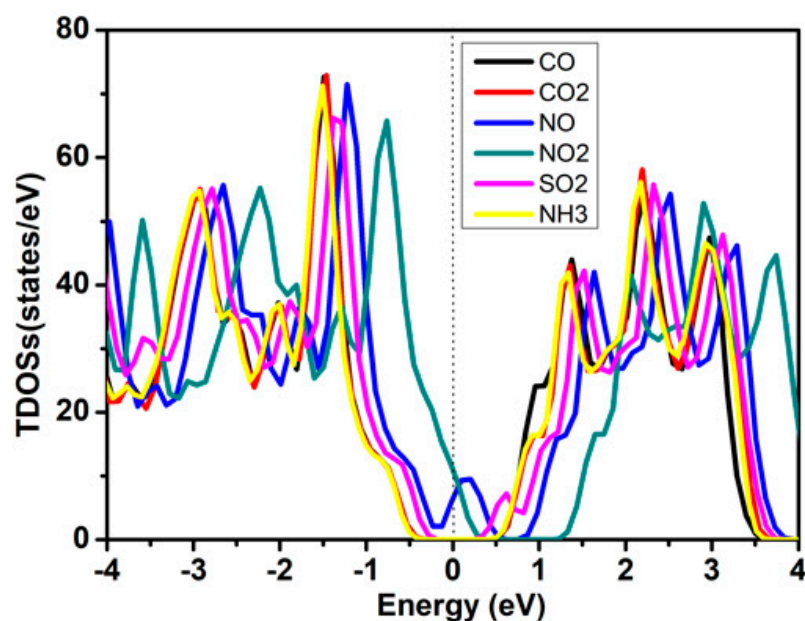
Figure 11. The total densities of states (TDOSs) derived from the PBE functional of the molecules adsorbed on the ZnSiP$_2$ monolayer.

3. Computational Methods

To find the lowest energy structure of 2D ZnSiP$_2$, a swarm-intelligence-based PSO method, implemented in CALYPSO code [52,53], combined with first-principles calculations, was employed, which has been used to successfully predict many 2D systems, such as Cu$_2$Si, PC$_6$, SnP$_3$, and B$_2$N$_3$ [19,34,54,55]. The structures of 2D ZnSiP$_2$ were searched with the simulation cells containing 1–4 formula units. The population size and the number of generations were both set to 30, which have been tested to give convergent results. In the first generation, a population of the structures was generated randomly. In the following generation, 60% of the population was generated from the lowest energy structures in the previous generation and all of the structures were fully relaxed, including the atomic positions and the lattice parameters.

The first-principles calculations based on density functional theory were performed using the projector-augmented wave (PAW) method, as implemented in VASP software [56–58]. The exchange correlation potential was described using Perdew–Burke–Ernzerhof (PBE) generalized gradient approximation [59] and corrected by the van der Waals (vdW) interaction in the calculation of the adsorption properties of ZnSiP$_2$. The plane-wave energy cut-off and Monkhorst–Pack K-point mesh density were set to 500 eV and $2\pi \times 0.03$ Å^{-1}, respectively. All geometries were optimized and relaxed until a total energy change smaller than 10^{-6} eV and a force tolerance acting on each atom less than 0.001 eVÅ^{-1} was achieved. In order to make the band-gap calculation more accurate for semiconductors, the HSE06 functional was employed [60]. A vacuum thickness of 25 Å was used to avoid the interlayer interactions. The nudged elastic band (NEB) method was used to obtain the K-ion diffusion energy barrier. To assess the dynamic stability, phonon spectra were calculated using the PHONOPY code [61]. In addition, ab initio molecular dynamics (AIMD) were explored with the NVT ensemble to examine the thermal stability.

In order to study the interactions between metals (gas molecules) and substrates, adsorption energies and adsorption distances were systematically calculated, according to the following equation:

$$E_{\text{ad}} = \frac{(E_{\text{total}} - nE_{\text{metal(gas)}} - E_{\text{ZnSiP}_2})}{n} \tag{1}$$

where E_{total}, E_{ZnSiP_2}, and $E_{metal(gas)}$ represent the total energy of the metal (gas molecules) adsorbed on the $ZnSiP_2$ monolayer, the perfect $ZnSiP_2$ monolayer, and the metal in the bulk metal or gas molecules, respectively, and n is the number of adsorbed metal atoms.

The adsorption stability of the K-ion layer on the $ZnSiP_2$ monolayer is estimated by average adsorption energy, which is calculated using the following formula:

$$E_{av} = \frac{E_{ntotal} - E_{(n-1)total} - mE_K}{m} \tag{2}$$

where E_{ntotal} and $E_{(n-1)total}$ refer to the total energies of the $ZnSiP_2$ monolayer with n and $(n-1)$ layers and m is the number of K atoms in every layer.

For a given concentration x of $K_xZn_2Si_2P_4$, the open-circuit voltage (OCV) can be obtained with the following equation:

$$V = \frac{E(x_2) - E(x_1) - (x_2 - x_1)E_K}{e(x_2 - x_1)} \tag{3}$$

where $E(x_2)$ and $E(x_1)$ are the total energies of $K_xZn_2Si_2P_4$ at two adjacent K-ion concentrations x_2 and x_1, e is the element charge, and E_K is the energy of one K atom in the bulk K metal.

The theoretical capacity can be evaluated from:

$$C_M = \frac{cF}{M} \tag{4}$$

where c is the number of adsorbed K atoms per $ZnSiP_2$ unit, F is the Faraday constant (26,801 mAhmol^{-1}), and M is the molar weight of $ZnSiP_2$ in gmol^{-1}.

4. Conclusions

In summary, we predicted the $ZnSiP_2$ monolayer as a new 2D semiconductor material which can be used as an anode material for K-ion batteries and NO_2 gas sensors by the global-optimization algorithm combined with first-principles calculation. Phonon simulation, molecular dynamics, and elastic-constant calculations confirmed its stability. The calculated electronic structure and mechanical properties indicate that $ZnSiP_2$ has an indirect band gap of 1.79 eV and exhibits anisotropic mechanical characteristics. Furthermore, we investigated 2D $ZnSiP_2$ as an anode for KIBs. The $ZnSiP_2$ monolayer has a theoretical capacity of 517 mAh/g for K-ions and a low diffusion barrier of 0.12 eV. In addition, we also investigated the gas-sensing properties of the $ZnSiP_2$ monolayer with six gas molecules (CO, CO_2, SO_2, NO, NO_2, and NH_3). The results show that the $ZnSiP_2$ monolayer is a promising gas sensor for NO_2 with high sensitivity and selectivity.

Author Contributions: Conceptualization, C.P. and D.Z.; formal analysis, C.P., Z.W. and X.T.; writing—original draft preparation, C.P.; writing—review and editing, D.Z. and J.C.; funding acquisition, D.Z., C.P. and J.C. All authors have read and agreed to the published version of the manuscript.

Institutional Review Board Statement: Not applicable.

Informed Consent Statement: Not applicable.

Data Availability Statement: Data available on request from the authors.

Conflicts of Interest: The authors declare no conflict of interest.

Sample Availability: Samples of the compounds are available on request from the authors.

References

1. Wang, Q.; Kalantar-Zadeh, K.; Kis, A.; Coleman, J.N.; Strano, M.S. Electronics and optoelectronics of two-dimensional transition metal dichalcogenides. *Nat. Nanotechnol.* **2012**, *7*, 699–712. [CrossRef]
2. Jana, S.; Thomas, S.; Chi, H.L.; Jun, B.; Sang, U.L. Rational design of a PC_3 monolayer: A high-capacity, rapidly charging anode material for sodium-ion batteries. *Carbon* **2020**, *157*, 420–426. [CrossRef]
3. Mayorga-Martinez, C.C.; Sofer, Z.; Pumera, M. Layered black phosphorus as a selective vapor sensor. *Angew. Chem.* **2015**, *54*, 14317–14320. [CrossRef]
4. Kumar, R.; Goel, N.; Kumar, M. UV-Activated MoS_2 based fast and reversible NO_2 sensor at room temperature. *ACS Sens.* **2017**, *2*, 1744–1752. [CrossRef]
5. Lin, J.; Yu, T.; Han, F.; Yang, G. Computational predictions of two-dimensional anode materials of metal-ion batteries. *Wiley Interdiscip. Rev. Comput. Mol. Sci.* **2020**, *10*, 1473. [CrossRef]
6. Kumar, V.; Azhikodan, D.; Roy, D.R. 2D Sb_2C_3 monolayer: A promising material for recyclable gas sensor for environmentally toxic nitrogen-containing gases (NCGs). *J. Hazard. Mater.* **2021**, *405*, 124168. [CrossRef]
7. Wang, G.; Pandey, R.; Karna, S.P. Carbon phosphide monolayers with superior carrier mobility. *Nanoscale* **2016**, *8*, 8819–8825. [CrossRef]
8. Guan, J.; Liu, D.; Zhu, Z.; Tomanek, D. Two-Dimensional phosphorus carbide: Competition between sp^2 and sp^3 bonding. *Nano Lett.* **2016**, *16*, 3247–3252. [CrossRef]
9. Singh, D.; Kansara, S.; Gupta, S.K.; Sonvane, Y. Single layer of carbon phosphide as an efficient material for optoelectronic devices. *J. Mater. Sci.* **2018**, *53*, 8314–8327. [CrossRef]
10. Li, F.; Liu, X.; Wang, J.; Zhang, X.; Yang, B.; Qu, Y.; Zhao, M. A promising alkali-metal ion battery anode material: 2D metallic phosphorus carbide (β_0-PC). *Electrochim. Acta* **2017**, *258*, 582–590. [CrossRef]
11. Qi, S.; Li, F.; Qu, Y.; Yang, Y.; Li, W.; Zhao, M. Prediction of a flexible anode material for Li/Na ion batteries: Phosphorous carbide monolayer (α-PC). *Carbon* **2019**, *141*, 444–450. [CrossRef]
12. Wang, J.; Lei, J.; Yang, G.; Xue, J.; Cai, Q.; Chen, D.; Lu, H.; Zhang, R.; Zheng, Y. An Ultra-Sensitive and selective nitrogen dioxide sensor based on novel P_2C_2 monolayer from theoretical perspective. *Nanoscale* **2018**, *10*, 21936–21943. [CrossRef] [PubMed]
13. Zhang, J.; Xu, L.; Yang, C.; Zhang, X.; Ma, L.; Zhang, M.; Lu, J. Two-dimensional single-layer PC_6 as promising anode materials for Li-ion batteries: The first-principles calculations study. *Appl. Surf. Sci.* **2020**, *510*, 145493. [CrossRef]
14. Lu, N.; Zhuo, Z.; Guo, H.; Wu, P.; Fa, W.; Wu, X.; Zeng, X.C. A new Two-dimensional functional material with desirable bandgap and ultrahigh carrier mobility. *J. Phys. Chem. Lett.* **2018**, *9*, 1728–1733. [CrossRef] [PubMed]
15. Jing, Y.; Ma, Y.; Li, Y.; Heine, T. GeP_3: A small indirect band gap 2D crystal with high carrier mobility and strong interlayer quantum confinement. *Nano Lett.* **2017**, *17*, 1833–1838. [CrossRef]
16. Yi, W.; Chen, X.; Wang, Z.; Ding, Y.; Yang, B.; Liu, X. A novel two-dimensional δ-InP_3 monolayer with high stability, tunable band gap, high carrier mobility, and gas sensing of NO_2. *J. Mater. Chem. C* **2019**, *7*, 7352–7359. [CrossRef]
17. Yu, T.; Zhao, Z.; Sun, Y.; Bergara, A.; Lin, J.; Zhang, S.; Xu, H.; Zhang, L.; Yang, G.; Liu, Y. Two-dimensional PC_6 with direct band gap and anisotropic carrier mobility. *J. Am. Chem. Soc.* **2019**, *141*, 1599–1605. [CrossRef]
18. Shen, Y.; Liu, J.; Li, X.; Wang, Q. Two-Dimensional T-$NiSe_2$ as a promising anode material for Potassium-ion batteries with low average voltage, high ionic conductivity, and superior carrier mobility. *ACS Appl. Mater. Interfaces* **2019**, *11*, 35661–35666. [CrossRef]
19. Li, J.; Wu, J.; Yu, Y. DFT exploration of sensor performances of two-dimensional WO_3 to ten small gases in terms of work function and band gap changes and *I-V* responses. *Appl. Surf. Sci.* **2021**, *546*, 149104. [CrossRef]
20. Chen, R.; Luo, S.; Xie, D.; Yu, Y.; Xiang, L. Highly dispersive palladium loading on ZnO by galvanic replacements with improved methane sensing performances. *Chemosensors* **2022**, *10*, 329. [CrossRef]
21. Beniwal, S.; Hooper, J.; Miller, D.P.; Costa, P.S.; Chen, G.; Liu, S.Y.; Dowben, P.A.; Sykes, E.C.H.; Zurek, E.; Enders, A. Graphene-like boron-carbon-nitrogen monolayers. *ACS Nano* **2017**, *11*, 2486–2493. [CrossRef] [PubMed]
22. Saini, H.; Das, S.; Pathak, B. BCN monolayer for high capacity Al-based dual-ion batteries. *Mater. Adv.* **2020**, *1*, 2418–2425. [CrossRef]
23. Pu, C.; Li, C.; Lv, L.; Zhou, D.; Tang, X. Structure and optoelectronic properties for two dimensional BCN from first-principles calculations. *Chin. J. Lumin.* **2020**, *41*, 48–55. [CrossRef]
24. Fu, X.; Guo, J.; Li, L.; Dai, T. Structural and electronic properties of predicting two-dimensional BC_2P and BC_3P_3 monolayers by the global optimization method. *Chem. Phys. Lett.* **2019**, *726*, 69–76. [CrossRef]
25. Tang, M.; Wang, C.; Schwingenschlogl, U.; Yang, G. BC_6P Monolayer: Isostructural and isoelectronic analogues of graphene with desirable properties for K-Ion batteries. *Chem. Mater.* **2021**, *33*, 9262–9269. [CrossRef]
26. Popov, V.P.; Pamplin, B.R. Epitaxial growth of solid solutions of $ZnSiP_2$ in Si. *J. Cryst. Growth* **1972**, *15*, 129–132. [CrossRef]
27. Martinez, A.D.; Miller, E.M.; Norman, A.G.; Schnepf, R.R.; Leick, N.; Perkins, C.; Stradins, P.; Toberer, E.S.; Tamdoli, A.C. Growth of amorphous and epitaxial $ZnSiP_2$–Si alloys on Si. *J. Mater. Chem. C* **2018**, *6*, 2696–2703. [CrossRef]
28. Martinez, A.D.; Warren, E.L.; Gorai, P.; Borup, K.A.; Kuciauskas, D.; Dippo, P.C.; Ortiz, B.R.; Macaluso, R.T.; Nguyen, S.D.; Greenaway, A.L.; et al. Solar energy conversion properties and defect physics of $ZnSiP_2$. *Energy Environ. Sci.* **2016**, *9*, 1031–1041. [CrossRef]

29. Scanlon, D.O.; Walsh, A. Bandgap engineering of ZnSnP$_2$ for high-efficiency solar cells. *Appl. Phys. Lett.* **2012**, *100*, 251911. [CrossRef]

30. Yuan, Y.; Zhu, X.; Zhou, Y.; Chen, X.; An, C.; Zhou, Y.; Zhang, R.; Gu, C.; Zhang, L.; Li, X.; et al. Pressure-engineered optical properties and emergent superconductivity in chalcopyrite semiconductor ZnSiP$_2$. *NPG Asia Mater.* **2021**, *13*, 15. [CrossRef]

31. Sreeparvathy, P.C.; Kanchana, V.; Vaitheeswaran, G. Thermoelectric properties of zinc based pnictide semiconductors. *J. Appl. Phys.* **2016**, *119*, 085701. [CrossRef]

32. Liu, J.; Emrys, T.; Miao, J.; Huang, Y.; Rondinelli, J.M.; Hendrik, H. Understanding chemical bonding in alloys and the representation in atomistic simulations. *J. Phys. Chem. C* **2018**, *122*, 14996–15009. [CrossRef]

33. Guan, J.; Zhu, Z.; Tománek, D. Phase coexistence and metal-insulator transition in few-layer phosphorene: A computational study. *Phys. Rev. Lett.* **2014**, *113*, 046804. [CrossRef] [PubMed]

34. Yang, L.M.; Bačić, V.; Popov, I.A.; Boldyrev, A.I.; Heine, T.; Frauenheim, T.; Ganz, E. Two-dimensional Cu$_2$Si monolayer with planar hexacoordinate copper and silicon bonding. *J. Am. Chem. Soc.* **2015**, *137*, 2757–2762. [CrossRef] [PubMed]

35. Wu, J.; Li, J.; Yu, Y. A theoretical analysis on the oxidation and water dissociation resistance on group-IV phosphide monolayers. *ChemPhysChem* **2020**, *21*, 2539–2549. [CrossRef] [PubMed]

36. Huang, B.; Zhuang, H.; Yoon, M.; Sumpter, B.G.; Wei, S. Highly stable two-dimensional silicon phosphides: Different stoichiometries and exotic electronic properties. *Phys. Rev. B* **2015**, *91*, 121401. [CrossRef]

37. Mouhat, F.; Couder, F.X. Necessary and sufficient elastic stability conditions in various crystal systems. *Phys. Rev. B* **2014**, *90*, 224104. [CrossRef]

38. Cadelano, E.; Palla, P.L.; Giordano, S.; Colombo, L. Elastic properties of hydrogenated grapheme. *Phys. Rev. B* **2010**, *82*, 235414. [CrossRef]

39. Wang, L.; Kutana, A.; Zou, X.; Yakobson, B.I. Electro-mechanical anisotropy of phosphorene. *Nanoscale* **2015**, *7*, 9746–9751. [CrossRef]

40. Cooper, R.C.; Lee, C.; Marianetti, C.A.; Wei, X.; Hone, J.; Kysar, J.W. Nonlinear elastic behavior of two-dimensional molybdenum disulfide. *Phys. Rev. B* **2013**, *87*, 035423. [CrossRef]

41. Yu, Y. High storage capacity and small volume change of potassium-intercalation into novel vanadium oxychalcogenide monolayers V$_2$S$_2$O, V$_2$Se$_2$O and V$_2$Te$_2$O: An ab initio DFT investigation. *Appl. Surf. Sci.* **2021**, *546*, 149062. [CrossRef]

42. Zhang, S.H.; Liu, B.G. Superior ionic and electronic properties of ReN$_2$ monolayers for Na-ion battery electrodes. *Nanotechnology* **2018**, *29*, 325401. [CrossRef] [PubMed]

43. Jiang, H.; Shyy, W.; Liu, M.; Wei, L.; Wu, M.; Zhao, T.S. Boron phosphide monolayer as a potential anode material for alkali metal-based batteries. *J. Mater. Chem. A* **2017**, *5*, 672–679. [CrossRef]

44. Dou, K.; Ma, Y.; Zhang, T.; Huang, B.; Dai, Y. Prediction of two-dimensional PC$_6$ as a promising anode material for potassium-ion batteries. *Phys. Chem. Chem. Phys.* **2019**, *21*, 26212–26218. [CrossRef]

45. Rehman, J.; Fan, X.; Laref, A.; Zheng, W.T. Adsorption and diffusion of potassium on 2D SnC sheets for potential high-performance anodic applications of potassium-ion batteries. *ChemElectroChem* **2020**, *7*, 3832–3838. [CrossRef]

46. Li, F.; Qu, Y.; Zhao, M. Germanium sulfide nanosheet: A universal anode material for alkali metal ion batteries. *J. Mater. Chem. A* **2016**, *4*, 8905–8912. [CrossRef]

47. Er, D.; Li, J.; Naguib, M.; Gogotsi, Y.; Shenoy, V. Ti$_3$C$_2$ MXene as a high capacity electrode material for metal (Li, Na, K, Ca) ion batteries. *ACS Appl. Mater. Interfaces* **2014**, *6*, 11173–11179. [CrossRef]

48. Xiang, P.; Sharma, S.; Wang, Z.M.; Wu, J.; Schwingenschlogl, U. Flexible C$_6$BN monolayers as promising anode materials for high-performance K-ion batteries. *ACS Appl. Mater. Interfaces* **2020**, *12*, 30731–30739. [CrossRef]

49. Yuan, X.; Chen, Z.; Huang, B.; He, Y.; Zhou, N. Potential application of MoS$_2$/M$_2$CS$_2$ (M = Ti, V) heterostructures as anode materials for metal-ion batteries. *J. Phys. Chem. C* **2021**, *125*, 10226–10234. [CrossRef]

50. Zhang, X.; Yu, Z.; Wang, S.S.; Guan, S.; Yang, H.Y.; Yao, Y.; Yang, S.A. Theoretical prediction of MoN$_2$ monolayer as a high capacity electrode material for metal ion batteries. *J. Mater. Chem. A* **2016**, *4*, 15224–15231. [CrossRef]

51. Joshi, R.; Ozdemir, B.; Peralta, J.; Barone, V. Hexagonal BC$_3$: A robust electrode material for Li, Na, and K ion batteries. *J. Phys. Chem. Lett.* **2015**, *6*, 2728–2732. [CrossRef]

52. Wang, Y.; Lv, J.; Zhu, L.; Ma, Y. CALYPSO: A method for crystal structure prediction. *Comput. Phys. Commun.* **2012**, *183*, 2063–2070. [CrossRef]

53. Wang, Y.; Lv, J.; Zhu, L.; Ma, Y. Crystal structure prediction via particle-swarm optimization. *Phys. Rev. B* **2010**, *82*, 094116–094118. [CrossRef]

54. Liu, C.; Yang, X.; Liu, J.; Ye, X. Theoretical prediction of two-dimensional SnP$_3$ as a promising anode material for Na-ion batteries. *ACS Appl. Energy Mater.* **2018**, *1*, 3850–3859. [CrossRef]

55. Lin, S.; Xu, M.; Hao, J.; Wang, X.; Wu, M.; Shi, J.; Cui, W.; Liu, D.; Lei, W.; Li, Y. Prediction of superhard B$_2$N$_3$ with two-dimensional metallicity. *J. Mater. Chem. C* **2019**, *7*, 4527–4532. [CrossRef]

56. Kresse, G.; Furthmüller, J. Efficiency of Ab initio total energy calculations for metals and semiconductors using a plane-wave basis set. *Comput. Mater. Sci.* **1996**, *6*, 15–50. [CrossRef]

57. Kresse, G.; Furthmüller, J. Efficient iterative schemes for Ab initio total-energy calculations using a plane-wave basis set. *Phys. Rev. B* **1996**, *54*, 11169–11186. [CrossRef] [PubMed]

58. Blöchl, P.E. Projector augmented-wave method. *Phys. Rev. B* **1994**, *50*, 17953–17979. [CrossRef] [PubMed]

59. Perdew, J.P.; Burke, K.; Ernzerhof, M. Generalized gradient approximation made simple. *Phys. Rev. Lett.* **1996**, *77*, 3865. [CrossRef]
60. Heyd, J.; Scuseria, G.E.; Ernzerhof, M. Hybrid functionals based on a screened coulomb potential. *J. Chem. Phys.* **2003**, *118*, 8207–8215. [CrossRef]
61. Togo, A.; Oba, F.; Tanaka, I. First-Principles calculations of the ferroelastic transition between rutile-Type and CaCl$_2$-Type SiO$_2$ at high pressures. *Phys. Rev. B* **2008**, *78*, 134106. [CrossRef]